An improved assembling algorithm in boundary elements with Galerkin weighting applied to three-dimensional Stokes flows

Sofia Sarraf[*]

Associate professor (UNCo)
Research associate (CONICET)
IITCI (UNCo-CONICET)
Buenos Aires 1400, (Q8300IBX) Neuquén, Argentina
Email: sofia.sarraf@fain.uncoma.edu.ar

Ezequiel López

Associate professor (UNCo)
Research associate (CONICET)
IITCI (UNCo-CONICET)
Buenos Aires 1400, (Q8300IBX) Neuquén, Argentina
Email: ezequiel.lopez@fain.uncoma.edu.ar

Laura Battaglia, Gustavo Ríos Rodríguez
Jorge D'Elía[†]

Associate professors (UTN, UNL, and UNL)
Senior Researchers (CONICET)
CIMEC (UNL-CONICET)
Predio CONICET-Santa Fe, Colectora RN 168
El Pozo, Santa Fe (3000), Argentina
Email: lbattaglia@santafe-conicet.gob.ar, gusadrr@santafe-conicet.gov.ar, jdelia@intec.unl.edu.ar

ABSTRACT

In the Boundary Element Method (BEM), the Galerkin weighting technique allows to obtain numerical solutions of a Boundary Integral Equation (BIE), giving the Galerkin Boundary Element Method (GBEM). In three-dimensional (3D) spatial domains, the nested double surface integration of GBEM leads to a significantly larger computational time for assembling the linear system than with the standard collocation method. In practice, the

---

[*]CONICET: Consejo Nacional de Investigaciones Científicas y Técnicas, UNCo: Universidad Nacional del Comahue, IITCI: Instituto de Investigación en Tecnologías y Ciencias de la Ingeniería.

[†]UNL: Universidad Nacional del Litoral, UTN: Universidad Tecnológica Nacional, CIMEC: Centro de Investigación de Métodos Computacionales, corresponding author.

computational time is roughly an order of magnitude larger, thus limiting the use of GBEM in 3D engineering problems. The standard approach for reducing the computational time of the linear system assembling is to skip integrations whenever possible. In this work, a modified assembling algorithm for the element matrices in GBEM is proposed for solving integral kernels that depend on the exterior unit normal. This algorithm is based on kernels symmetries at the element level and not on the flow nor in the mesh. It is applied to a BIE that models external creeping flows around 3D closed bodies using second-order kernels, and it is implemented using OpenMP. For these BIEs, the modified algorithm is on average 32% *faster than the original one. Keywords: Complex Flows, Computational Fluid Dynamics, Microfluidics, Newtonian Flows*

1 Introduction

As is well known, the Boundary Element Method (BEM) is based on the formulation of a boundary value problem of elliptic type as a Boundary Integral Equation (BIE) [1, 2].

Two standard discretization procedures of a BIE are the point collocation technique, and the Galerkin weighting method (GBEM, Galerkin BEM). Examples of weighted residual techniques in a BIE include the symmetric boundary element method [3], the symmetric Galerkin boundary element method (SGBEM) [4–6], and the variational boundary element method [7], among others. In the case of kernels with a weak singularity, there are analytical expressions of the double surface integrals as, for instance, the potential integrals in computational electromagnetics, which are designed for flat triangles but restricted to kernels with a linear or constant density layer in the numerator [8]. More recently, Carley [9] has proposed a method for evaluating potential integrals on planar triangular elements using a polar coordinate decomposition, with explicit formulas for the regular, principal value, and finite part integrals.

In classical formulations of the collocation and the Galerkin weighting techniques, every element interacts with the others, leading to dense influence matrices. The computation of these matrices involves a cost $O(M^2)$, where M is the number of degrees of freedom. The influence matrix for each pair of elements in GBEM requires the computation of double surface interaction integrals with a weak singularity, which are solved in this work with an extension of the scheme proposed by Taylor [10], where a systematic way for handling double surface integrals over flat triangular elements is developed. The strategy is based on a convenient reordering of the four iterate integrations that moves the weak singularity to the origin of the four-dimensional Euclidean space and then systematically applies the Duffy transformation [10], i.e. regularizes the integrand by using polar coordinates. Taylor uses a Gauss–Legendre numerical quadrature on three coordinates and performs an analytic integration in the fourth one. However, since the Taylor scheme is restricted to wave propagation kernels in computational electromagnetics, a modification was proposed in [11, 12], where the fourth analytic integration of the Taylor scheme is replaced by a numerical quadrature in order to handle kernels with a weak singularity under a general framework.

The assembly of the system matrix for GBEM is performed by means of a double loop over the whole set of elements. In three-dimensional (3D) spatial domains, this double loop leads to a significantly greater computational time for assembling the linear system than with the collocation technique. The time ratio needed for assembling the matrix with collocation and GBEM is roughly one order of magnitude. This fact has severely limited the use of GBEM in 3D engineering problems [13].

The standard approach for reducing the computational time in the assembling of the linear system is to avoid integrations whenever possible. However this can be difficult to perform in mixed BIEs where some kernel components depend on the exterior unit normal. In general, the double loop for the linear system assembly can not be eliminated, although it is plausible to take advantage of block symmetries at the level of the element matrix, which is computed as a double surface integral where its integrand is a double matrix product. Other relationships between coefficient matrices in SGBEM for two-dimensional scalar problems were given in [14]. The aim of this work is to propose a strategy able to reduce the computational time in the assembly stage through schemes that use the kernel symmetries in GBEM. In particular, the 3D creeping flow kernel is addressed, which is used in the modeling of several flow problems such as micro-electromechanical systems (MEMS) simulation [15, 16], peristaltic transport in microfluidic channels [17–19], among others. The proposed method is implemented using OpenMP on a multi-core computer [20].

The work is organized as follows. First, the GBEM technique is reviewed for a BIE of the Fredholm type and second kind, with mixed and weakly singular second-order tensor kernels. Then, due to symmetries of the Green function, the proposed scheme which takes advantage of the block symmetries at the element matrix level is presented. The numerical examples include flow problems with analytic or numerical solutions taken from the literature.

2 The Power-Miranda/Hebeker integral formulation

The Power-Miranda/Hebeker integral formulation (or PMH-IF for short) consists in a BIE without rigid modes for the Stokes flow around a rigid, closed, piecewise smooth surface A in $\mathbb{R}^3$, and it can be classified as a Completed Indirect Velocity BIE (CIV-BIE) [21], or Completed Double-Layer BIE (CDL-BIE) [1, 22]. In this section, Cartesian tensor notation is used, i.e. the indices i, j, k have the values $1, 2, 3$ and correspond to the Cartesian coordinates (x, y, z), respectively. An indirect integral formulation for the Stokes equation leads to consider the single-layer $\tilde{S}_{ij}(\boldsymbol{x}, \boldsymbol{y})$ and the double-layer $\tilde{K}_{ij}(\boldsymbol{x}, \boldsymbol{y})$ kernels. For the steady flow case these kernels are given by [1, 22]

$$\tilde{S}_{ij}(\boldsymbol{x}, \boldsymbol{y}) = \frac{1}{8\pi\mu}\left[\frac{\delta_{ij}}{r} + \frac{r_i r_j}{r^3}\right] \tag{1a}$$

$$\tilde{K}_{ij}(\boldsymbol{x}, \boldsymbol{y}) = -\frac{3}{4\pi}\frac{r_i r_j r_k}{r^5} n_k(\boldsymbol{y}) \tag{1b}$$

where $\boldsymbol{r} = \boldsymbol{x} - \boldsymbol{y}$ and $r = \|\boldsymbol{x} - \boldsymbol{y}\|_2$, with the integration and field points $\boldsymbol{y} = (y_1, y_2, y_3)$ and $\boldsymbol{x} = (x_1, x_2, x_3)$, respectively (see Fig. 1, left), while $n_k = n_k(\boldsymbol{y})$ is the unit normal to the surface A at point $\boldsymbol{y}$, δ_{ij} is the Kronecker delta, $\|\cdot\|_2$ is the Euclidean norm for vectors, μ is the dynamic viscosity of the fluid, and the Einstein summation convention over repeated indices is

employed. For oscillatory Stokes flow the kernels adopt the following expressions [22]

$$\tilde{S}_{ij}(\boldsymbol{x},\boldsymbol{y}) = \frac{1}{8\pi\mu}\left[\frac{\delta_{ij}}{r}\mathcal{A}(s) + \frac{r_i r_j}{r^3}\mathcal{B}(s)\right] \tag{2a}$$

$$\tilde{K}_{ij}(\boldsymbol{x},\boldsymbol{y}) = -\frac{1}{4\pi}\left\{\frac{(\delta_{ij}r_k + \delta_{kj}r_i)}{r^3}c_1(s) + \frac{\delta_{ik}r_j}{r^3}c_2(s) + \frac{r_i r_j r_k}{r^5}c_3(s)\right\}n_k(\boldsymbol{y}) \tag{2b}$$

in which

$$\mathcal{A}(s) = 2e^{-s}\left(1+\frac{1}{s}+\frac{1}{s^2}\right) - \frac{2}{s^2} \tag{3a}$$

$$\mathcal{B}(s) = -2e^{-s}\left(1+\frac{3}{s}+\frac{3}{s^2}\right) + \frac{6}{s^2} \tag{3b}$$

$$c_1(s) = e^{-s}(s+1) - \mathcal{B}(s) \tag{3c}$$

$$c_2(s) = 1 - \mathcal{B}(s) \tag{3d}$$

$$c_3(s) = 5\mathcal{B}(s) - 2e^{-s}(s+1) \tag{3e}$$

where $s = r\sqrt{-I\Omega/\nu}$ is the non-dimensional distance, $\Omega = 2\pi f$ is the circular frequency of the oscillation, $\nu = \mu/\rho$ is the kinematic viscosity of the fluid, and I is the imaginary unit, while f is the frequency in Hz, and ρ is the fluid density. The PMH-IF uses both single and double layer densities, and it can be written as [22]

$$u_i(\boldsymbol{x}) = \int_A \left[\tilde{K}_{ij}\psi_j(\boldsymbol{x}) - \tilde{H}_{ij}\psi_j(\boldsymbol{y})\right]\, \mathrm{d}A_{\boldsymbol{y}}, \quad \text{for all } \boldsymbol{x} \in A \tag{4}$$

where $\psi_j(\boldsymbol{x})$ is the double-layer surface density, and $u_i(\boldsymbol{x})$ is the unperturbed flow velocity. The differential surface element is denoted as $\mathrm{d}A_{\boldsymbol{y}} = \mathrm{d}A(\boldsymbol{y})$ (see Fig. 1, left). Besides, the PMH kernel $\tilde{H}_{ij}(\boldsymbol{x},\boldsymbol{y})$ is given by

$$\tilde{H}_{ij}(\boldsymbol{x},\boldsymbol{y}) = \tilde{K}_{ij}(\boldsymbol{x},\boldsymbol{y}) + \chi_H \tilde{S}_{ij}(\boldsymbol{x},\boldsymbol{y}) \tag{5}$$

where χ_H is an arbitrary positive parameter that was introduced by Hebeker [22] in order to couple the single layer density $\boldsymbol{\phi}$ with the double-layer density $\boldsymbol{\psi}$. To this end, Hebeker defines $\boldsymbol{\phi}(\boldsymbol{x}) = \chi_H\, \boldsymbol{\psi}(\boldsymbol{x})$. This coupling allows to remove the six rigid modes of the classic BIE through the *ad-hoc* introduction of the kernel $\tilde{S}_{ij}(\boldsymbol{x},\boldsymbol{y})$. In addition, it accounts for both, the global force and the global torque over the closed surface [1,22]. In the analysis presented by Hebeker based on an iterative solution

of the linear equation system, it is concluded that $\chi_H = 1$ is a good choice with respect to the conditioning of the equation system, which will be used in the present work. Nevertheless, it should be noted that only a direct solution of the equation system is considered in all examples. Since the right hand side of Eqn. (4) is a datum, this case reduces to a Fredholm BIE of second kind with weakly singular kernels for $\psi_j(\boldsymbol{x})$. Regarding the symmetry of the single- and double- layer kernels in the case of the steady flow case, given by Eqn. (1a-1b), they can be summarized as $\tilde{K}_{ij}(\boldsymbol{x},\boldsymbol{y}) = \tilde{K}_{ji}(\boldsymbol{x},\boldsymbol{y})$ and $\tilde{S}_{ij}(\boldsymbol{x},\boldsymbol{y}) = \tilde{S}_{ji}(\boldsymbol{x},\boldsymbol{y})$.

3 Numerical formulation

In order to solve Eqn. (4), a Galerkin BEM is considered. The technique uses a nested double loop over the elements $p,q = 1,2,...,E$, where E is the number of elements (or panels) in the BEM mesh, and points $\boldsymbol{x}$, $\boldsymbol{y}$ are linked to the elements p,q, respectively (see Fig. 1, left). In this section, the values of the variables at the element level are denoted with superscripts, while nodal values are indicated by subscripts, and superindex T denotes a transposed array. Moreover, the notation $\int \mathrm{d}z \int \mathrm{d}y \int \mathrm{d}x \int \mathrm{d}w\, f(w,x,y,z)$ is used instead of $\int\int\int\int f(w,x,y,z)\ \mathrm{d}w\,\mathrm{d}x\,\mathrm{d}y\,\mathrm{d}z$, where the integrations are performed from right to left.

3.1 Galerkin weighting technique using linear elements

The standard Galerkin weighting technique uses the shape functions $\boldsymbol{N}_\gamma(\boldsymbol{x})$, for $\gamma = 1,2,...,N$, being N the number of mesh nodes, in order to minimize the error through orthogonality conditions whenever a BIE is discretized. When this technique is applied to Eqn. (4), the following linear equation system is obtained

$$\sum_{p=1}^{E}\sum_{q=1}^{E}\left[\boldsymbol{I}^{(p,q)}\boldsymbol{\psi}^{(p)} - \boldsymbol{J}^{(p,q)}\boldsymbol{\psi}^{(q)}\right] = \sum_{p=1}^{E}\boldsymbol{M}^{(p)}\boldsymbol{u}^{(p)} \tag{6}$$

where the next notation is used for the element matrices

$$\boldsymbol{I}^{(p,q)} = \int_{A^{(p)}}\mathrm{d}A_{\boldsymbol{x}}\int_{A^{(q)}}\mathrm{d}A_{\boldsymbol{y}}\left[\boldsymbol{N}^{(p)T}(\boldsymbol{x})\,\tilde{\boldsymbol{K}}(\boldsymbol{x},\boldsymbol{y})\,\boldsymbol{N}^{(p)}(\boldsymbol{x})\right] \tag{7}$$

and

$$\boldsymbol{J}^{(p,q)} = \int_{A^{(p)}}\mathrm{d}A_{\boldsymbol{x}}\int_{A^{(q)}}\mathrm{d}A_{\boldsymbol{y}}\left[\boldsymbol{N}^{(p)T}(\boldsymbol{x})\,\tilde{\boldsymbol{H}}(\boldsymbol{x},\boldsymbol{y})\,\boldsymbol{N}^{(q)}(\boldsymbol{y})\right] \tag{8}$$

while the source vector at the element level is given by

$$\boldsymbol{M}^{(p)}\boldsymbol{u}^{(p)} = \int_{A^{(p)}} \mathrm{d}A_{\boldsymbol{x}} \left[\boldsymbol{N}^{(p)T}(\boldsymbol{x})\boldsymbol{N}^{(p)}(\boldsymbol{x})\right] \boldsymbol{U}^{(p)} \tag{9}$$

3.2 Surface integrals over flat triangles in GBEM

Flat triangles with 3 nodes (T1 elements) are employed as boundary elements. The global numbering of nodes in triangles p and q is denoted with i,j,k and r,s,t, respectively (see Fig. 1, right). The element vectors for the solution field in Eqn. (6) are written as

$$\underset{9\times1}{\boldsymbol{\psi}^{(p)}} = \begin{bmatrix} \boldsymbol{\psi}_i \\ \boldsymbol{\psi}_j \\ \boldsymbol{\psi}_k \end{bmatrix} \text{ and } \underset{9\times1}{\boldsymbol{\psi}^{(q)}} = \begin{bmatrix} \boldsymbol{\psi}_r \\ \boldsymbol{\psi}_s \\ \boldsymbol{\psi}_t \end{bmatrix}, \text{ with } \underset{3\times1}{\boldsymbol{\psi}_m} = \begin{bmatrix} \psi_{3m-2} \\ \psi_{3m-1} \\ \psi_{3m} \end{bmatrix} \tag{10}$$

respectively, where m denotes any of the nodes i,j,k and r,s,t, while the element source is given by

$$\underset{9\times1}{\boldsymbol{U}^{(p)}} = \begin{bmatrix} \boldsymbol{U}_i \\ \boldsymbol{U}_j \\ \boldsymbol{U}_k \end{bmatrix}, \text{ with } \underset{3\times1}{\boldsymbol{U}_m} = \begin{bmatrix} U_{3m-2} \\ U_{3m-1} \\ U_{3m} \end{bmatrix} \tag{11}$$

Equations (7-8) provide the element interaction integrals, which have a weak singularity $O(1/r)$. In order to compute Eqns. (7-8), an extended Taylor integration scheme is employed [10–12], with a full numerical quadrature on the four coordinates in order to handle the weak singularity with a general framework. For this aim, two sets of coordinates are introduced, one for each simplex: (ξ_1,ξ_2) over panel p, and (η_1,η_2) over panel q (see Fig. 1, right)

$$(\xi_1,\xi_2) : 0 \le \xi_1 \le 1 \; ; \; 0 \le \xi_2 \le \xi_1 \tag{12a}$$

$$(\eta_1,\eta_2) : 0 \le \eta_1 \le 1 \; ; \; 0 \le \eta_2 \le \eta_1 \tag{12b}$$

The generic point coordinates are transformed into those of the panels p and q using the following expressions

$$\boldsymbol{x}(\xi_1,\xi_2) = \boldsymbol{N}^{(p)}(\xi_1,\xi_2)\, \boldsymbol{x}^{(p)} \tag{13a}$$

$$\boldsymbol{y}(\eta_1,\eta_2) = \boldsymbol{N}^{(q)}(\eta_1,\eta_2)\, \boldsymbol{y}^{(q)} \tag{13b}$$

with the element shape functions

$$\underset{3\times 9}{\boldsymbol{N}^{(p)}}(\boldsymbol{\xi}) = \begin{bmatrix} \boldsymbol{N}_i^{(p)}(\boldsymbol{\xi}) & \boldsymbol{N}_j^{(p)}(\boldsymbol{\xi}) & \boldsymbol{N}_k^{(p)}(\boldsymbol{\xi}) \end{bmatrix} \tag{14a}$$

$$\underset{3\times 9}{\boldsymbol{N}^{(q)}}(\boldsymbol{\eta}) = \begin{bmatrix} \boldsymbol{N}_r^{(q)}(\boldsymbol{\eta}) & \boldsymbol{N}_s^{(q)}(\boldsymbol{\eta}) & \boldsymbol{N}_t^{(q)}(\boldsymbol{\eta}) \end{bmatrix} \tag{14b}$$

and the nodal coordinates of the vertices of each triangle

$$\boldsymbol{x}^{(p)} = \begin{bmatrix} \boldsymbol{x}_i & \boldsymbol{x}_j & \boldsymbol{x}_k \end{bmatrix}^T \quad \text{and} \quad \boldsymbol{y}^{(q)} = \begin{bmatrix} \boldsymbol{y}_r & \boldsymbol{y}_s & \boldsymbol{y}_t \end{bmatrix}^T \tag{15}$$

In Eqns. (14a-14b)

$$\underset{3\times 3}{\boldsymbol{N}_\alpha^{(p)}}(\boldsymbol{\xi}) = \text{diag}\left(\begin{bmatrix} N_\alpha^{(p)}(\boldsymbol{\xi}) & N_\alpha^{(p)}(\boldsymbol{\xi}) & N_\alpha^{(p)}(\boldsymbol{\xi}) \end{bmatrix} \right) \tag{16a}$$

$$\underset{3\times 3}{\boldsymbol{N}_\beta^{(q)}}(\boldsymbol{\eta}) = \text{diag}\left(\begin{bmatrix} N_\beta^{(q)}(\boldsymbol{\eta}) & N_\beta^{(q)}(\boldsymbol{\eta}) & N_\beta^{(q)}(\boldsymbol{\eta}) \end{bmatrix} \right) \tag{16b}$$

for $\alpha = i, j, k$ in the p element, and $\beta = r, s, t$ in the q element, see Fig. 1 (right), and

$$\begin{aligned} N_i^{(p)}(\boldsymbol{\xi}) &= (1-\xi_1) & N_r^{(q)}(\boldsymbol{\eta}) &= (1-\eta_1) \\ N_j^{(p)}(\boldsymbol{\xi}) &= (\xi_1-\xi_2) & N_s^{(q)}(\boldsymbol{\eta}) &= (\eta_1-\eta_2) \\ N_k^{(p)}(\boldsymbol{\xi}) &= \xi_2 & N_t^{(q)}(\boldsymbol{\eta}) &= \eta_2 \end{aligned} \tag{17}$$

Thereby, the element interaction integrals, Eqns. (7-8), are written as

$$\boldsymbol{I}^{(p,q)} = \boldsymbol{J}^{(p)}\boldsymbol{J}^{(q)}\ \hat{\boldsymbol{I}}^{(p,q)} \tag{18a}$$

$$\boldsymbol{J}^{(p,q)} = \boldsymbol{J}^{(p)}\boldsymbol{J}^{(q)}\ \hat{\boldsymbol{J}}^{(p,q)} \tag{18b}$$

where $J^{(p)} = 2A^{(p)}$ is the Jacobian of panel p, $A^{(p)}$ being its area, and the same notation applies to panel q. Therefore, the element interaction integrals can be expressed in simplex coordinates as follows

$$\begin{aligned}\hat{\boldsymbol{I}}^{(p,q)} = &\int_0^1 \mathrm{d}\xi_1 \int_0^{\xi_1} \mathrm{d}\xi_2 \int_0^1 \mathrm{d}\eta_1 \int_0^{\eta_1} \mathrm{d}\eta_2 \\ &\times \boldsymbol{N}^{(p)T}(\boldsymbol{\xi})\, \tilde{\boldsymbol{K}}(\boldsymbol{x}(\boldsymbol{\xi}), \boldsymbol{y}(\boldsymbol{\eta}))\, \boldsymbol{N}^{(p)}(\boldsymbol{\xi})\end{aligned} \tag{19}$$

and

$$\begin{aligned}\hat{\boldsymbol{J}}^{(p,q)} = &\int_0^1 \mathrm{d}\xi_1 \int_0^{\xi_1} \mathrm{d}\xi_2 \int_0^1 \mathrm{d}\eta_1 \int_0^{\eta_1} \mathrm{d}\eta_2 \\ &\times \boldsymbol{N}^{(p)T}(\boldsymbol{\xi})\, \tilde{\boldsymbol{H}}(\boldsymbol{x}(\boldsymbol{\xi}), \boldsymbol{y}(\boldsymbol{\eta}))\, \boldsymbol{N}^{(q)}(\boldsymbol{\eta})\end{aligned} \tag{20}$$

Further details about the evaluation of Eqns. (19-20) with a weak singularity using an extended Taylor scheme are given in [10–12], and summarized in Appendix A.

4 Assembly of the element interaction integrals

The computation of Eqns. (19-20) must be performed for each pair of interacting elements $p, q = 1, 2, ..., E$, and therefore, it would be desirable to avoid integrations whenever possible. Moreover, the evaluation of Eqns. (7-8) has many quantities in common and hence, every pair of these integrals can be computed together. Nevertheless, the evaluation of Eqns. (7-8), in general, does not give a symmetric global matrix for the discrete problem. In this section, some assembling strategies are considered.

4.1 Basic assembly A0

The basic assembly (A0) is taken as reference for analyzing the performance improvements of the other methods introduced in this work, and it is formulated without any optimization. It consists in the standard matrix product, without taking into account the fact that the element nodal matrices $\boldsymbol{N}_{\alpha}^{(p)}(\boldsymbol{\xi})$ and $\boldsymbol{N}_{\beta}^{(q)}(\boldsymbol{\eta})$ are diagonal. The integrands in Eqns. (19-20) have the general form

$$\underset{9\times 9}{\boldsymbol{F}^{(p,q)}}(\boldsymbol{\xi}, \boldsymbol{\eta}) = \begin{bmatrix} \mathcal{F}_{i,r}^{(p,q)} & \mathcal{F}_{i,s}^{(p,q)} & \mathcal{F}_{i,t}^{(p,q)} \\ \mathcal{F}_{j,r}^{(p,q)} & \mathcal{F}_{j,s}^{(p,q)} & \mathcal{F}_{j,t}^{(p,q)} \\ \mathcal{F}_{k,r}^{(p,q)} & \mathcal{F}_{k,s}^{(p,q)} & \mathcal{F}_{k,t}^{(p,q)} \end{bmatrix} \tag{21}$$

where

$$\underset{3\times3}{\mathcal{F}^{(p,q)}_{\alpha,\beta}}(\boldsymbol{\xi},\boldsymbol{\eta}) = \begin{cases} \underset{3\times3}{\boldsymbol{N}^{(p)}_{\alpha}}(\boldsymbol{\xi})\underset{3\times3}{\tilde{\boldsymbol{K}}_{\alpha,\beta}}(\boldsymbol{\xi},\boldsymbol{\eta})\underset{3\times3}{\boldsymbol{N}^{(p)}_{\beta}}(\boldsymbol{\xi}), & \text{for } \boldsymbol{I}^{(p,q)} \\ \underset{3\times3}{\boldsymbol{N}^{(p)}_{\alpha}}(\boldsymbol{\xi})\underset{3\times3}{\tilde{\boldsymbol{H}}_{\alpha,\beta}}(\boldsymbol{\xi},\boldsymbol{\eta})\underset{3\times3}{\boldsymbol{N}^{(q)}_{\beta}}(\boldsymbol{\eta}), & \text{for } \boldsymbol{J}^{(p,q)} \end{cases} \tag{22}$$

and

$$\underset{3\times3}{\tilde{\boldsymbol{K}}_{\alpha,\beta}}(\boldsymbol{\xi},\boldsymbol{\eta}) = \begin{bmatrix} \tilde{K}_{3\alpha-2,3\beta-2} & \tilde{K}_{3\alpha-2,3\beta-1} & \tilde{K}_{3\alpha-2,3\beta} \\ \tilde{K}_{3\alpha-1,3\beta-2} & \tilde{K}_{3\alpha-1,3\beta-1} & \tilde{K}_{3\alpha-1,3\beta} \\ \tilde{K}_{3\alpha,3\beta-2} & \tilde{K}_{3\alpha,3\beta-1} & \tilde{K}_{3\alpha,3\beta} \end{bmatrix} \tag{23}$$

for $\alpha = i,j,k$ in the p element, and $\beta = r,s,t$ in the q element.

4.2 Reduced assembly A1

The reduced assembly 1 (A1) is obtained when the diagonal nature of the element shape functions $\boldsymbol{N}^{(p)}_{\alpha}(\boldsymbol{\xi})$ and $\boldsymbol{N}^{(q)}_{\beta}(\boldsymbol{\eta})$ is taken into account, regardless of whether the BIE has (or not) a symmetric kernel, reducing the matrix product to

$$\underset{3\times3}{\mathcal{F}^{(p,q)}_{\alpha,\beta}}(\boldsymbol{\xi},\boldsymbol{\eta}) = \begin{cases} \underset{\mathbb{R}}{\mathrm{N}^{(\mathrm{p})}_{\alpha}}(\boldsymbol{\xi})\ \underset{3\times3}{\tilde{\boldsymbol{K}}_{\alpha,\beta}}(\boldsymbol{\xi},\boldsymbol{\eta})\ \underset{\mathbb{R}}{\mathrm{N}^{(\mathrm{p})}_{\beta}}(\boldsymbol{\xi})\ \text{, for } \boldsymbol{I}^{(p,q)} \\ \underset{\mathbb{R}}{\mathrm{N}^{(\mathrm{p})}_{\alpha}}(\boldsymbol{\xi})\ \underset{3\times3}{\tilde{\boldsymbol{H}}_{\alpha,\beta}}(\boldsymbol{\xi},\boldsymbol{\eta})\ \underset{\mathbb{R}}{\mathrm{N}^{(\mathrm{q})}_{\beta}}(\boldsymbol{\eta})\ \text{, for } \boldsymbol{J}^{(p,q)} \end{cases} \tag{24}$$

4.3 Reduced assembly A2

The reduced assembly 2 (A2) is obtained from the A1 when the symmetry of the double-layer kernel $\tilde{K}_{ij}(\boldsymbol{x},\boldsymbol{y})$ is considered, resulting in

$$\underset{9\times9}{\mathcal{F}^{(p,q)}}(\boldsymbol{\xi},\boldsymbol{\eta}) = \begin{bmatrix} \mathcal{F}^{(p,q)}_{i,r}(\boldsymbol{\xi},\boldsymbol{\eta}) & \mathcal{F}^{(p,q)}_{i,s}(\boldsymbol{\xi},\boldsymbol{\eta}) & \mathcal{F}^{(p,q)}_{i,t}(\boldsymbol{\xi},\boldsymbol{\eta}) \\ \mathcal{F}^{(p,q)}_{j,r}(\boldsymbol{\xi},\boldsymbol{\eta}) & \mathcal{F}^{(p,q)}_{j,s}(\boldsymbol{\xi},\boldsymbol{\eta}) & \mathcal{F}^{(p,q)}_{j,t}(\boldsymbol{\xi},\boldsymbol{\eta}) \\ \mathcal{F}^{(p,q)}_{k,r}(\boldsymbol{\xi},\boldsymbol{\eta}) & \mathcal{F}^{(p,q)}_{k,s}(\boldsymbol{\xi},\boldsymbol{\eta}) & \hat{\mathcal{F}}^{(p,q)}_{k,t}(\boldsymbol{\xi},\boldsymbol{\eta}) \end{bmatrix} \tag{25}$$

with $\mathcal{F}^{(p,q)}_{j,r}(\boldsymbol{\xi},\boldsymbol{\eta}) = \mathcal{F}^{(p,q)}_{i,s}(\boldsymbol{\xi},\boldsymbol{\eta})$, $\mathcal{F}^{(p,q)}_{k,r}(\boldsymbol{\xi},\boldsymbol{\eta}) = \mathcal{F}^{(p,q)}_{i,t}(\boldsymbol{\xi},\boldsymbol{\eta})$, and $\mathcal{F}^{(p,q)}_{k,s}(\boldsymbol{\xi},\boldsymbol{\eta}) = \mathcal{F}^{(p,q)}_{j,t}(\boldsymbol{\xi},\boldsymbol{\eta})$. As a summary, a sketch of the symmetries in the element matrices of T1 elements that are induced by the symmetries of the single and double layer kernels

for the Stokes equation, is shown in Fig. 2 (bottom).

4.4 Operation count in the assemblies A0, A1, and A2

The basic element matrix product, given by Eqns. (19-20), defines a standard treatment without any optimization in the programming of the element matrices. Therefore, it is not what it should be implemented in a production code. Nevertheless, it can be chosen as a reference for some comparisons. Table 1 contains the estimates of the number of operations (products and sums) by Gauss-Legendre quadrature point involved in the evaluation of the A0, A1, and A2 assemblies, where the count is performed according to the coding of the matrix product. However, since the matrix products are performed inside the nested double loop $p,q = 1,2,...,E$ and inside the quadruple loop of numerical quadrature, in practice the percentage of reduction will degrade with respect to those indicated in Tab. 1. It should be noted that for the case of the double-layer kernel $\tilde{K}_{ij}(\boldsymbol{x},\boldsymbol{y})$, given by Eqn. (1b), the reduced assembly A2, given by Eqn. (25), applies.

5 Numerical examples

The aim of the examples is to show the time savings when the assembling algorithm which takes advantage of the block symmetries at the element matrix level is applied. In the first and second examples, the wall times for the three assembling techniques are compared as functions of the degrees of freedom number M. The remaining examples are introduced to show the benefits of applying the assembling strategies in problems with intricate geometries. The numerical solutions computed with GBEM are validated with other numerical methods, as in [23]. In all the examples, a Q_{22} quadrature rule is employed, where the first subindex denotes the number of Gauss-Legendre (GL) quadrature points in each surface coordinate used for the self-integral and for the first layer of neighboring elements, and the second subindex is the number of GL quadrature points used for the remaining layers [23]. The examples are computed on an I7-3930K processor with six cores, using real or complex double precision, GFortran compiler, and main optimization flags -Ofast -march=native -fwhole-file -fwhole-program -Warray-temporaries. In all cases, the linear systems are solved with a direct method through the DGESVX and ZGESVX routines from a LAPACK library based on the multi-thread ATLAS. These routines also give the reciprocal of the system matrix condition number rcond, but at the price of one copy of such matrix. In the numerical examples LAPACK/ATLAS gives a peak of 112 GFlops, while the HPL benchmark throws 122 GFlops, both in double precision. The LAPACK/ATLAS and HPL software are freely available at the NETLIB repository (http://www.netlib.org). Also valgrind and gprof were used in the preliminary tests. Regarding the computation of the system matrix, the M columns are distributed among the available threads using the OpenMP directive parallel region, while the do loops are executed in parallel by the team of threads, where the shared arrays are synchronized using critical and flush directives. In order to verify the multi-thread assembly, it was checked that the linear systems obtained with one or more threads are equal to machine precision.

5.1 Steady Stokes flow around the unit sphere

This test consists in the steady creeping flow around the unit sphere (radius $R = 1\,\mathrm{m}$) [24–27]. The unperturbed stream has velocity $\boldsymbol{U} = (1,0,0) \times 10^{-4}\,\mathrm{m/s}$, while the dynamic viscosity of the fluid is $\mu = 10^{-3}\,\mathrm{Pa \cdot s}$ and its density is $\rho = 1\,\mathrm{kg/m^3}$.

This is a classical test in the literature about Stokes flow simulation [1], and the numerical results computed with the GBEM technique, e.g. the traction field on the sphere surface, were validated in [23]. The absolute value of the relative error $|e_r|$ for the Stokes force is computed as $|e_r| = |F_{\text{num}}/F_{\text{analytic}} - 1|$, with $F_{\text{analytic}} = F_S$ and $F_S = 6\pi\mu UR$ is the (steady) Stokes force. In Fig. 3 the following magnitudes are plotted as functions of the degrees of freedom number $M = 3N$: (i) the reciprocal of the condition numbers of the system matrices rcond (left), (ii) the relative errors $|e_r\%|$ in the Stokes force (middle left), (iii) the wall times required with the assemblies A0-A2 and collocation CO (middle right), and (iv) the relative wall times between the A1 and A0 assemblies, and between the A2 and A1 ones (right). It can be seen that there is an average reduction in the wall times of approximately $100 - 51 = 49$ % for A1 with respect to A0, and $100 - 68 = 32$ % for A2 with respect to A1.

5.2 Oscillatory Stokes flow around the unit sphere

This test consists in the oscillatory creeping flow [28, 29] around the unit sphere (radius $R = 1\,\text{m}$). The unperturbed stream has amplitude $\boldsymbol{U} = (1,0,0) \times 10^{-4}\,\text{m/s}$, the dynamic viscosity of the fluid is $\mu = 10^{-3}\,\text{Pa}\cdot\text{s}$, its density is $\rho = 1\,\text{kg/m}^3$, while the oscillation frequency is $f = 10^{-2}\,\text{Hz}$. In this case, the kernel given by Eqn. (2b) is not symmetric, although it tends to be symmetric as the frequency $\Omega \to 0$. Therefore, only the A1 can be applied. The absolute value of the relative error $|e_r|$ for the Stokes force is computed as $|e_r| = |F_{\text{num}}/F_{\text{analytic}} - 1|$, with $F_{\text{analytic}} = F_S(1 + \zeta + \zeta^2/3)$ when the sphere is at rest and the fluid is oscillating [22], where $\zeta = R\sqrt{-I\Omega/\nu}$ and F_s is the steady Stokes force. In Fig. 4 the following magnitudes are plotted as functions of the degrees of freedom number $M = 3N$: (i) the reciprocal of the condition numbers of the system matrices rcond (left), (ii) the relative errors $|e_r\%|$ in the Stokes force (middle left), (iii) the wall times required for the assemblies A0-A1 (GBEM), and collocation BEM (CO) (middle right), and (iv) the relative wall times between the A0-A1 assemblies (right). As in the previous example, it can be seen that there is an average reduction in the wall times of approximately: $100 - 51 = 49$ % for A1 with respect to A0.

5.3 Stokes flow around bodies with edges and corners

Three closed bodies with edges and corners are considered [23]: a hollow cube, a sculpted sphere, and a perforated plate, each of them immersed in a creeping flow of a viscous fluid of Newtonian type. They are meshed using the NETGEN mesher [30]. The fluid density is $\rho = 1\ \text{kg/m}^3$, while the kinematic viscosity is $\nu = 1\ \text{m}^2/\text{s}$. In the first two cases, an uniform steady flow around each body has incoming velocity of $U_\infty = 0.001$ m/s along the x_1 direction.

5.3.1 Hollow cube

The hollow cube (HC) [30] is obtained when the unit cube is intersected by a sphere and by a complement of a sphere, where the x_1 direction coincides with one of the symmetry axis of the cube. The mesh shown in Fig. 5 (left) has 4 904 nodes and 9 824 elements. The wall times required for assembling the system matrix are given in Table 2 (left sub-columns).

5.3.2 Sculpted sphere

The sculpted sphere (SS) [30] is obtained when the unit sphere is intersected by a smaller one and by three cylinders oriented according to the coordinate axes. The mesh shown in Fig. 5 (middle) has 6 062 nodes and 12 128 elements. When the undisturbed flow is aligned along, for instance, the x_1 Cartesian axis, the flow is not symmetrical. Furthermore, the mesh is not symmetric. The wall times required for assembling the system matrix are given in Table 2 (middle sub-columns).

5.3.3 Perforated plate

This is an application case and consists in the oscillatory Stokes flow around a Perforated Plate (PP) that oscillates perpendicularly to a fixed substrate [31]. This case was validated using finite elements through the PETSc-FEM code [32]. It is a 3D intricate geometry which is frequently used in MEMS in order to reduce the dissipation of energy due to the air damping. The plate is made of polysilicon and the gap between the upper plate and the substrate is $4\,\mu$m. The plate dimensions are: length $L = L_x = 300\,\mu$m, width $B = L_y = 100\,\mu$m, and height $H = L_z = 2\,\mu$m. The height of the substrate is $10\,\mu$m, and the plate has 75 equidistant circular holes with $4\,\mu$m in radius. The micro-beam is double clamped, at its left end $x = 0$ and at its right end $x = L_x$. The maximum amplitude of the harmonic vibration is $\tilde{A} = 1$ μm and it is produced at the center of the micro-beam. The dynamic viscosity of air is $\mu = 1.86 \times 10^{-11}$ kg/(μm s). The oscillation frequency is $f = 17\,600$ Hz. The mesh shown in Fig. 5 (right) has 8 697 nodes and 17 686 elements. The wall times required for assembling the system matrix in this case, are given in Table 2 (right sub-columns).

5.4 Collocation BEM vs. GBEM

Regarding a comparison between collocation BEM and GBEM, in [11] the folowing properties were stated when they are appplied to BIEs such as the PMH-IF for the Stokes equation in the steady case: (i) in GBEM, the size of the solution vector is $3N$, while it is $3E$ in collocation BEM. Since $N \ll E$ for BEM meshes immersed in 3D domains, then the GBEM is less expensive than collocation BEM in core-memory resources, especially when dense matrices are employed, therefore, in general, a GBEM approach allows to use more refined meshes for a given size of the core memory; (ii) the system matrix with GBEM is symmetric (in the steady case), whereas with collocation BEM it is not; (iii) the net forces obtained with GBEM are more accurate than those obtained with collocation BEM; and (iv) GBEM exhibits monotonic convergence while collocation BEM does not. For example, comparisons between GBEM and collocation BEM applied to the Stokes flow around the unit sphere are shown in Fig. 6 for the steady flow using the reduced assemblies A0-A2 and collocation BEM (CO), and in Fig. 7 for the oscillatory flow using the reduced assemblies A0-A1 and CO.

6 Conclusions

The harnessing of symmetries in the element interaction integrals in Galerkin BEM can be introduced into a standard implementation through minor changes at the element level. According to the test cases solved in this work, it can be concluded that a meaningful reduction in the wall time needed for assembling the system matrix can be reached using the reduced assembly strategy A2. On average, it is found to be $100 - 68 = 32\%$ faster than the A1 procedure. The reduced assembly A2

is based on block symmetries at the element level which are due to symmetries of the kernels and do not depend on those of the flow nor of the mesh. The examples with intricate geometries allow to conclude that the reduction in the computation time for the assembly process is almost independent of the mesh details.

Acknowledgments This work has received financial support from CONICET (Argentina, grant PIP 112-20111-978), UNL (Argentina, grant CAI+D 2011-01-00134-LI, CAI+D 2011-01-00012-LI), ANPCyT (Argentina, grants PICT 2660–14, PICT-E 0191–14, and PICT 0938–13), UNCo (Argentina, grant 04/I-215), and was performed with the Free Software Foundation/GNU-Project resources as Linux OS and GFortran, as well as other Open Source resources such as NETGEN and OpenDX.

References

[1] Power, H., and Wrobel, L. C., 1995. *Boundary Integral Methods in Fluid Mechanics*. Computational Mechanics Publications, Southampton,UK.

[2] D'Elía, J., Storti, M. A., and Idelsohn, S. R., 1999. "A panel-Fourier method for free surface flows". *ASME J. Fluids Eng.,* **122**(2), Nov, pp. 309–317.

[3] Terravecchia, S., 2012. "Revisited mixed-value method via symmetric BEM in the substructuring approach". *Eng. Anal. with Boundary Elements,* **36**(12), pp. 1865–1882.

[4] Zhao, Z., and Yuan, W., 2004. "Evaluation of singular integrals in the symmetric Galerkin boundary element method". *Adv. Eng. Software,* **35**(12), pp. 781–789.

[5] Sutradhar, A., Paulino, G. H., and Gray, L. J., 2008. *Symmetric Galerkin Boundary Element Method*. Springer.

[6] Salvadori, A., 2010. "Analytical integrations in 3D BEM for elliptic problems: evaluation and implementation". *Int. J. for Num. Meth. in Engng.,* **84**(5), pp. 505–542.

[7] Alia, A., M., S., and Erchiqui, F., 2006. "Variational boundary element acoustic modelling over mixed quadrilateral–triangular element meshes". *Comm. Numer. Meth. Engng.,* **22**(7), July, pp. 767–780.

[8] Sievers, D., Eibert, T. F., and Hansen, V., 2005. "Correction to "On the calculation of potential integrals for linear source distributions on triangular domains"". *IEEE Trans. on Antennas and Propag.,* **53**(9), pp. 3113–3113.

[9] Carley, M. J., 2013. "Analytical formulae for potential integrals on triangles". *J. Appl. Mech.,* **80**(4), July, pp. 041008–041008–7.

[10] Taylor, D. J., 2003. "Accurate and efficient numerical integration of weakly singulars integrals in Galerkin EFIE solutions". *IEEE Trans. on Antennas and Propag.,* **51**(7), July, pp. 1630–1637.

[11] D'Elía, J., Battaglia, L., Cardona, A., and Storti, M., 2011. "Full numerical quadrature of weakly singular double surface integrals in Galerkin boundary element methods". *Int. J. for Num. Meth. in Biomedical Engng.,* **27**(2), pp. 314–334.

[12] Sarraf, S., López, E., Ríos Rodríguez, G., and D'Elía, J., 2014. "Validation of a Galerkin technique on a boundary integral equation for creeping flow around a torus". *Comp. Appl. Math.,* **33**(1), pp. 63–80.

[13] Iemma, U., 2010. "On the use of a SIMD vector extension for the fast evaluation of Boundary Element Method

coefficients". *Adv. Eng. Software,* **41**(3), pp. 451–463.

[14] Yu, G. Y., 2003. "Relationship among coefficient matrices in symmetric Galerkin boundary element method for two-dimensional scalar problems". *J. of App. Mech.,* **70**(4), pp. 479–486.

[15] Mukherjee, S., Telukunta, S., and Mukherjee, Y. X., 2005. "BEM modeling of damping forces on MEMS with thin plates". *Eng. Anal. Bound. Elem.,* **29**, pp. 1000–1007.

[16] Fachinotti, V., Cardona, A., D'Elía, J., and Paquay, S., 2007. "BEM for the analysis of fluid flow around MEMS". In Mecánica Computacional, vol. XXIV, Asociación Argentina de Mecánica Computacional (AMCA), pp. 1104–1119.

[17] Bandopadhyay, A., Tripathi, D., and Chakraborty, S., 2016. "Electroosmosis-modulated peristaltic transport in microfluidic channels". *Phys. Fluids,* **28**(5).

[18] Tripathi, D., Brushan, S., and Anwar Beg, O., 2016. "Transverse magnetic field driven modification in unsteady peristaltic transport with electrical double layer effects". *Colloids and Surfaces A: Physicochemical and Engineering Aspects,* **506**, pp. 32–39.

[19] Tripathi, D., Yadav, A., and Anwar Beg, O., 2017. "Electro-kinetically driven peristaltic transport of viscoelastic physiological fluids through a finite length capillary: Mathematical modeling". *Mathematical Biosciences,* **283**, pp. 155–168.

[20] Diaz, J., Muñoz Caro, C., and Niño, A., 2012. "A survey of parallel programming models and tools in the multi and many-core era". *IEEE Trans. Parallel Distr. Syst.,* **23**(8), pp. 1369–1388.

[21] Ingber, M. S., and Mammoli, A. A., 1999. "A comparison of integral formulations for the analysis of low Reynolds number flows". *Eng. Anal. Bound. Elem.,* **23**, pp. 307–315.

[22] Pozrikidis, C., 1997. *Boundary Integral and Singularity Methods for Linearized Viscous Flow*. Cambridge University Press.

[23] D'Elía, J., Battaglia, L., Cardona, A., Storti, M., and Ríos Rodríguez, G., 2014. "Galerkin boundary elements for a computation of the surface tractions in exterior Stokes flows". *ASME J. Fluids Eng.,* **136**(11), Sep, pp. 111102–111117.

[24] Tripathi, D., 2011. "Numerical study on creeping flow of Burgersfluids through a peristaltic tube". *ASME J. Fluids Eng.,* **133**(12), pp. 121104–121104–9.

[25] Wang, Z., Zhao, J., and Wu, J., 2014. "Stokes flow characteristics in a cylindrical quadrant duct with rotating outer wall". *ASME J. Fluids Eng.,* **136**(11), pp. 111202–111202–11.

[26] Lepchev, D., and Weihs, D., 2010. "Low Reynolds number flow in spiral microchannels". *ASME J. Fluids Eng.,* **132**(7), p. 071202.

[27] Hewson, R. W., 2009. "Free surface model derived from the analytical solution of Stokes flow in a wedge". *ASME J. Fluids Eng.,* **131**(4), pp. 041205–041205–5.

[28] Wang, C. Y., 2016. "Exact solutions for starting and oscillatory flows in an equilateral triangular duct". *ASME J. Fluids Eng.,* **138**(8), pp. 084503–084503–4.

[29] Ishikawa, T., and Vladimirov, V. A., 2015. "A stepping microrobot controlled by flow oscillations". *ASME J. Fluids Eng.,* **137**(8), pp. 084501–084501–3.

[30] Schöberl, J., 1997. "NETGEN - an advancing front 2D/3D-mesh generator based on abstract rules". *Comput Visual*

Sci, **1**(1), pp. 41–52.

[31] Xiao, J., and Ye, W., 2011. "Wavelet BEM for large-scale Stokes flows based on the direct integral formulation". *Int. J. for Num. Meth. in Engng.,* **88**(7), pp. 693–714.

[32] Paz, R. R., Storti, M. A., Dalcin, L. D., Castro, H. G., and Kler, P. A., 2012. "FastMat: a C++ library for multi-index array computations". *Adv. Eng. Software,* **54**, pp. 38–48.

[33] Gray, L. J., and Griffith, B. E., 1998. "A faster Galerkin boundary integral algorithm". *Comm. Numer. Meth. Engng.,* **14**, pp. 1109–1117.

[34] Morino, L., 1985. *Computational Methods in Potential Aerodynamics*. Springer-Verlag.

[35] Landweber, L., 1961. *Handbook of Fluid Dynamics*. McGraw-Hill, ch. Motion of Immersed and Floating Bodies.

Appendix A: The extended Taylor scheme

Without loss of generality, Eqns. (18a-18b) can be written as

$$\boldsymbol{I} = \int_0^1 \mathrm{d}\xi_1 \int_0^{\xi_1} \mathrm{d}\xi_2 \int_0^1 \mathrm{d}\eta_1 \int_0^{\eta_1} \mathrm{d}\eta_2 \, \boldsymbol{f}(\boldsymbol{\xi},\boldsymbol{\eta}) \tag{26}$$

The Taylor strategy to evaluate Eqn. (26) is designed specifically for flat simple triangles p and q when they are contiguous or coincidents, and the integrand $\boldsymbol{f}(\boldsymbol{\xi},\boldsymbol{\eta})$ has a weak singularity. In that case, the relative coordinates $\mu_1 = \eta_1 - \xi_1$ and $\mu_2 = \eta_2 - \xi_2$ are introduced. The replacement of these coordinates into Eqn. (26) leads to

$$\boldsymbol{I} = \int_0^1 \mathrm{d}\xi_1 \int_{-\xi_1}^{1-\xi_1} \mathrm{d}\mu_1 \int_0^{\xi_1} \mathrm{d}\xi_2 \int_{-\xi_2}^{\mu_1+\xi_1-\xi_2} \mathrm{d}\mu_2 \, \boldsymbol{f}(\boldsymbol{\xi},\boldsymbol{\mu}) \tag{27}$$

Changing the integration order $(\mu_2,\xi_2,\mu_1,\xi_1)$ to the order $(\xi_2,\xi_1,\mu_2,\mu_1)$, combining integrals that have overlapping domains, and introducing several Duffy coordinate transformations, Eqn. (26) is split into 3, 6 and 1 independent integrals for the common facets, common edge, and common vertex cases, respectively. It should be noted that the new integration order moves the weak singularity to the origin, the overlapping domains occur in the plane of the relative coordinates (μ_1,μ_2), while the Duffy coordinate transformations regularize the integrands by using polar coordinates, and the selected ones are the same used by Taylor. In principle, there are 6 independent integrals in each case, although, with further considerations in the common facet and common vertex cases, they are reduced to 3 and 1, respectively. The final expressions are given in the next sections, where the following notations are used: $\tilde{\boldsymbol{f}}_n = \tilde{\boldsymbol{f}}(\boldsymbol{\xi}_n,\boldsymbol{\eta}_n)$, where $\tilde{\boldsymbol{f}}(\boldsymbol{\xi}_n,\boldsymbol{\eta}_n) = \boldsymbol{f}(\boldsymbol{\xi}_n,\boldsymbol{\eta}_n) + \boldsymbol{f}(\boldsymbol{\eta}_n,\boldsymbol{\xi}_n)$, and $\boldsymbol{\eta}_n = \boldsymbol{\xi}_n + \boldsymbol{\mu}_n$.

Common facets

In the case of flat common facets, Taylor found that the symmetry reduces the number of integrals from six to three, given by Eqn. (28)

$$\boldsymbol{I} = \sum_{n=1}^{3} \boldsymbol{I}_n \quad \text{with} \quad \boldsymbol{I}_n = \int_0^1 \mathrm{d}\omega \int_0^1 \mathrm{d}x \int_0^1 \mathrm{d}\chi_1 \int_0^1 \mathrm{d}\chi_2 \;\; \tilde{J}_n \tilde{\boldsymbol{f}}_n \tag{28}$$

where $(\omega, x, \chi_1, \chi_2)$ are the GL quadrature points, while $\boldsymbol{\xi}_n = \boldsymbol{\xi}_n(\omega, x, \chi_1, \chi_2) = (\xi_1, \xi_2)_n$, and $\boldsymbol{\mu}_n = \boldsymbol{\mu}_n(\omega, x, \chi_1, \chi_2) = (\mu_1, \mu_2)_n$, where the intervals $0 \leq \omega, x, \chi_1, \chi_2 \leq 1$ are the usual unit interval for the GL quadrature points. The coordinates $\boldsymbol{\mu}_n$ and $\boldsymbol{\xi}_n$ are computed using rows 1-2 and 3-4 of Table 3, respectively, and the Jacobian is obtained as $\tilde{J}_n = J_a J_n$, with $J_a = \omega$, while J_n is given in the row 5 of Table 3.

Common edge

In the case of a common edge, six integrals must be computed, and given by Eqn. (29)

$$\boldsymbol{I} = \sum_{n=4}^{9} \boldsymbol{I}_n \quad \text{with} \quad \boldsymbol{I}_n = \int_0^1 \mathrm{d}\omega \int_0^1 \mathrm{d}x_1 \int_0^1 \mathrm{d}x_2 \int_0^1 \mathrm{d}\chi_1 \;\; \tilde{J}_n \tilde{\boldsymbol{f}}_n \tag{29}$$

where the intervals $0 \leq \omega, x_1, x_2, \chi_1 \leq 1$ are the usual unity interval for the GL quadrature points. The coordinates $\boldsymbol{\mu}_n$ and $\boldsymbol{\xi}_n$ are computed using columns 1-2 and 3-4 of Table 4, respectively, and the Jacobian is obtained as $\tilde{J}_n = J_b \bar{J}$, with $J_b = x_1 \omega^2$ and $\bar{J} = 1 - \omega$.

Common vertex

Finally, in the case of a common vertex, the six integrals are reduced to one, and given by Eqn. (30)

$$\boldsymbol{I}_{10} = \int_0^1 \mathrm{d}\omega \int_0^1 \mathrm{d}z_1 \int_0^1 \mathrm{d}z_2 \int_0^1 \mathrm{d}z_3 \;\; \tilde{J}_{10} \tilde{\boldsymbol{f}}_{10} \tag{30}$$

where the intervals $0 \leq \omega, z_1, z_2, z_3 \leq 1$ are the usual unity interval for the GL quadrature points. The coordinates $\boldsymbol{\xi}_{10}$ and $\boldsymbol{\eta}_{10}$ are computed using columns 1-2 and 3-4 of Table 5, respectively, and the Jacobian is obtained as $\tilde{J}_{10} = J_c$, with $J_c = z_2 \omega^3$.

Appendix B: a BIE with a scalar kernel

In order to show the application of the proposed assembling algorithm to others cases aside from the Stokes flow, this appendix includes results for a BIE with a scalar kernel.

Reduced assembly A3

The reduced assembly A2 cannot be applied to BIEs with scalar kernels like those related to the Laplace or Helmholtz equations. Nevertheless, other symmetries can be taken into account. For instance, in [33] it is taken into account that the matrices of interaction between any pair of elements $p-q$ share the same geometric quantities except, in general, the unit normals $\boldsymbol{n}(\boldsymbol{x})$ and $\boldsymbol{n}(\boldsymbol{y})$, therefore it is convenient to compute both matrices simultaneously. This kind of strategy defines the reduced assembly A3 that can be used in BIEs with a scalar kernel, as the Morino Integral Formulation [34] (or Morino-IF for short).

The Morino integral formulation

The Morino-IF consists in a BIE for the exterior Neumann problem of the Laplace equation over a rigid, closed, piecewise smooth surface A in $\mathbb{R}^3$ [34] that can be written as

$$\frac{1}{2}\lambda(\boldsymbol{x}) - \int_A \tilde{D}(\boldsymbol{x},\boldsymbol{y})\lambda(\boldsymbol{y})\ \mathrm{d}A_{\boldsymbol{y}} = \int_A \tilde{C}(\boldsymbol{x},\boldsymbol{y})\ \sigma(\boldsymbol{x})\ \mathrm{d}A_{\boldsymbol{y}} \tag{31}$$

for all $\boldsymbol{x} \in A$, where $\lambda(\boldsymbol{x})$ is the double-layer surface density, and $\sigma(\boldsymbol{x})$ is the single-layer surface density. The single-layer $\tilde{C}(\boldsymbol{x},\boldsymbol{y})$ and the double-layer $\tilde{D}(\boldsymbol{x},\boldsymbol{y})$ kernels for the Laplace equation are given by $\tilde{C}(\boldsymbol{x},\boldsymbol{y}) = \hat{c}/r$, and $\tilde{D}(\boldsymbol{x},\boldsymbol{y}) = -\hat{c}r_k n_k(\boldsymbol{y})/r^3$, where $\hat{c} = 1/(4\pi)$. In addition, $\sigma(\boldsymbol{x}) = -U_k(\boldsymbol{x})n_k(\boldsymbol{x})$ is the value needed to cancel the component of the velocity in the normal direction to the surface A. In this way, the right hand side of Eq. (31) is given and, hence, the Morino-IF is reduced to a Fredholm BIE of second kind with weakly singular kernels for $\lambda(\boldsymbol{x})$.

Galerkin weighting technique for the Morino-IF

The application of the Galerkin weighting to Eq. (31), using T1 elements and after algebraic handling, leads to the linear equation system

$$\sum_{p=1}^{E}\sum_{q=1}^{E}\left[\frac{1}{6}A^{(p)}\delta^{(p,q)}\boldsymbol{I}_3 - \mathcal{L}^{(p,q)}\right]\boldsymbol{\lambda}^{(q)} = \sum_{p=1}^{E}\sum_{q=1}^{E} Q^{(p,q)}\boldsymbol{\sigma}^{(q)} \tag{32}$$

where $\delta^{(p,q)}$ is the Kronecker delta, $\boldsymbol{I}_3$ is the 3×3 identity matrix, and

$$\mathcal{L}^{(p,q)} = \int_{A^{(p)}} \mathrm{d}A_{\boldsymbol{x}} \int_{A^{(q)}} \mathrm{d}A_{\boldsymbol{y}} \left[\boldsymbol{N}^{(p)T}(\boldsymbol{x})\ \tilde{D}(\boldsymbol{x},\boldsymbol{y})\ \boldsymbol{N}^{(q)}(\boldsymbol{y})\right] \tag{33}$$

is the elemental matrix of the system, while the corresponding elemental matrix for the load term is given by

$$Q^{(p,q)} = \int_{A^{(p)}} \mathrm{d}A_{\boldsymbol{x}} \int_{A^{(q)}} \mathrm{d}A_{\boldsymbol{y}} \left[\boldsymbol{N}^{(p)T}(\boldsymbol{x})\, \tilde{C}(\boldsymbol{x},\boldsymbol{y})\, \boldsymbol{N}^{(q)}(\boldsymbol{y}) \right] \tag{34}$$

The elemental vectors for the solution and the right hand side of Eq. (32) are

$$\boldsymbol{\lambda}^{(q)} = \begin{bmatrix} \lambda_r \\ \lambda_s \\ \lambda_t \end{bmatrix} \qquad \text{and} \qquad \boldsymbol{\sigma}^{(q)} = \begin{bmatrix} \sigma_r \\ \sigma_s \\ \sigma_t \end{bmatrix} \tag{35}$$

respectively. In this case, the interaction matrix of p element (nodes i,j,k) with a q element (nodes r,s,t), see Fig. 1 (left), has the form

$$\underset{3\times 3}{\mathcal{L}^{(p,q)}} = \begin{bmatrix} \mathcal{L}_{i,r}^{(p,q)} & \mathcal{L}_{i,s}^{(p,q)} & \mathcal{L}_{i,t}^{(p,q)} \\ \mathcal{L}_{j,r}^{(p,q)} & \mathcal{L}_{j,s}^{(p,q)} & \mathcal{L}_{j,t}^{(p,q)} \\ \mathcal{L}_{k,r}^{(p,q)} & \mathcal{L}_{k,s}^{(p,q)} & \mathcal{L}_{k,t}^{(p,q)} \end{bmatrix} \tag{36}$$

and the elemental interaction matrix of the q element with the p element, has the form

$$\underset{3\times 3}{\mathcal{L}^{(q,p)}} = \begin{bmatrix} \mathcal{L}_{r,i}^{(q,p)} & \mathcal{L}_{r,j}^{(q,p)} & \mathcal{L}_{r,k}^{(q,p)} \\ \mathcal{L}_{s,i}^{(q,p)} & \mathcal{L}_{s,j}^{(q,p)} & \mathcal{L}_{s,k}^{(q,p)} \\ \mathcal{L}_{t,i}^{(q,p)} & \mathcal{L}_{t,j}^{(q,p)} & \mathcal{L}_{t,k}^{(q,p)} \end{bmatrix} \tag{37}$$

Equations (36-37) involves many common geometric operations except the unit normals $\boldsymbol{n}(\boldsymbol{x})$ (on the p element) and $\boldsymbol{n}(\boldsymbol{y})$ (on the q element). The reduced assembly A3 computes $\mathcal{L}^{(p,q)}$ and $\mathcal{L}^{(q,p)}$ simultaneously by a pair of nested loops $q = 1,2,...,E$ and $p = q, q+1, ..., E$, evaluating only once all the magnitudes that are shared, plus the unit normals $\boldsymbol{n}(\boldsymbol{x})$ and $\boldsymbol{n}(\boldsymbol{y})$.

Numerical example: Rankine closed body

This test consists in the steady potential flow around a Rankine closed body [35] aligned with the unperturbed stream $\boldsymbol{U} = (1,0,0)$ m/s, modeled with a source $+\Upsilon$ and a sink $-\Upsilon$ located at $(-a,0,0)$ and $(+a,0,0)$, respectively, with $a = 1$ m, both with the same strength $\Upsilon = 0.5$ m^3/s. The meshes are obtained using a conformal transformation of each mesh defined over the unit sphere. The analytic solution [35] is given by $\lambda = Q(1/s_- - 1/s_+)$, with $Q = \Upsilon/(4\pi)$, $s_\pm = \sqrt{(x \pm a)^2 + r^2}$,

where x is the axisymmetric coordinate and r is the radial one. In Fig. 8 the following magnitudes are plotted as functions of the degrees of freedom number $M = N$: (i) the reciprocal of the condition numbers of the system matrices (left) (ii) the Mean Squared Error MSE% in the dipolar density λ (middle left), (iii) the wall times with the assemblies A0, A1, A3 and collocation CO (middle right), and (iv) the relative wall times between the A1 and A0 assemblies, and between the A3 and A1 ones (right). It can be seen that there is a reduction in the wall times of approximately: $100 - 71 = 29$ % for A1 with respect to A0, and $100 - 53 = 47$ % for A3 with respect to A1.

List of Figures

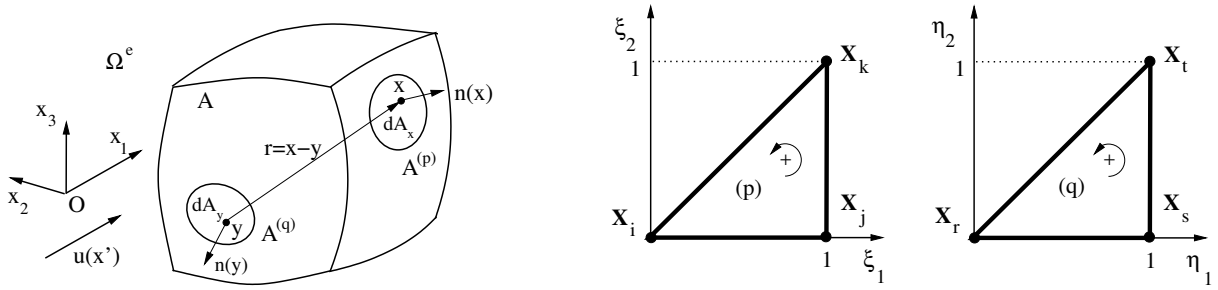

Fig. 1. Left: a rigid, closed, piecewise smooth surface A with an exterior domain Ω^e: field point $\boldsymbol{x}$, source point $\boldsymbol{y}$, relative position $\boldsymbol{r} = \boldsymbol{x} - \boldsymbol{y}$, unit normals $\boldsymbol{n}(\boldsymbol{x}), \boldsymbol{n}(\boldsymbol{y})$, and differential areas $\mathrm{d}A_{\boldsymbol{x}}$, $\mathrm{d}A_{\boldsymbol{y}}$. Right: master triangles p and q for the simplex coordinates

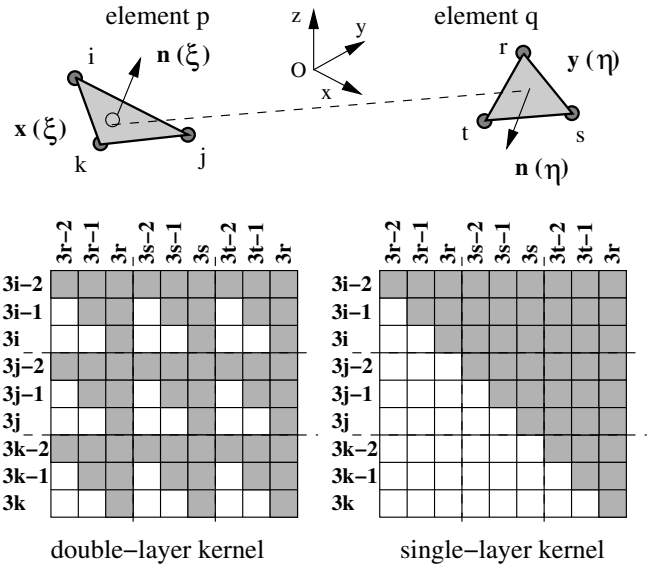

Fig. 2. The element matrices for the Stokes equation in 3D domains using T1 elements (top): (i) double layer kernel $\hat{\mathcal{K}}^{(p,q)}(\boldsymbol{x}(\boldsymbol{\xi}),\boldsymbol{y}(\boldsymbol{\eta}))$, symmetric in each 3x3 block (bottom left); (ii) single-layer kernel $\hat{\mathcal{S}}^{(p,q)}(\boldsymbol{x}(\boldsymbol{\xi}),\boldsymbol{y}(\boldsymbol{\eta}))$: symmetric with respect to the main diagonal (bottom right).

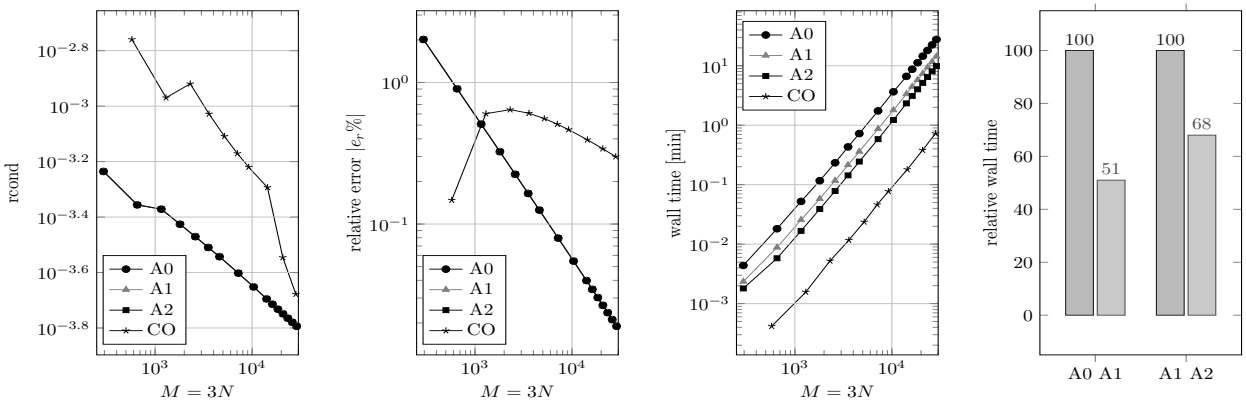

Fig. 3. Steady Stokes flow. Assemblies A0-A2 and collocation CO, as functions of the degrees of freedom number $M = 3N$: (i) the reciprocal of the condition numbers of the system matrices rcond (left), (ii) the relative errors $|e_r\%|$ in the Stokes force (middle left), (iii) the wall times required for assemblies A0-A2, and collocation CO (middle right), and (iv) the relative wall times between the A1 and A0 assemblies, and between the A2 and A1 ones (right).

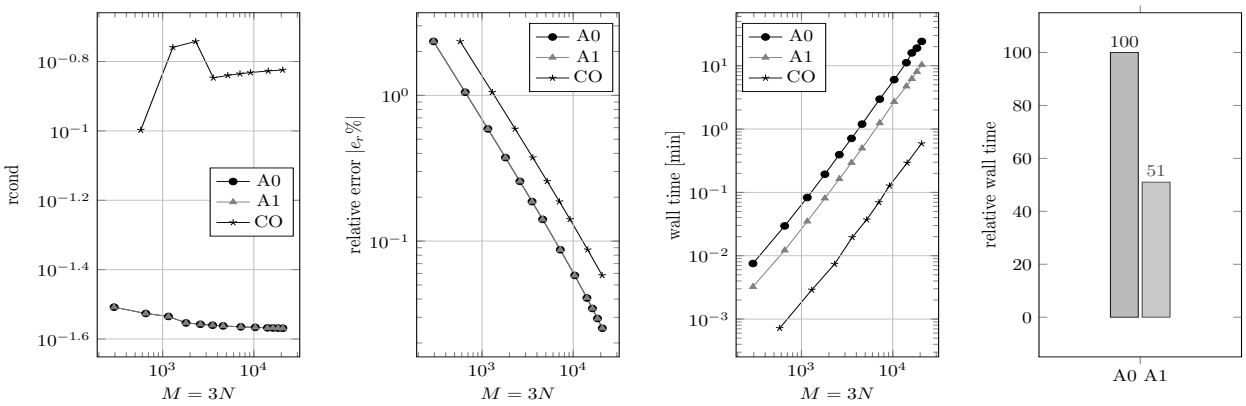

Fig. 4. Oscillatory Stokes flow. Assemblies A0-A1 and collocation CO, as functions of the degrees of freedom number $M = 3N$: (i) the reciprocal of the condition numbers of the system matrices rcond (left), (ii) the relative errors $|e_r\%|$ in the Stokes force (middle left), (iii) the wall times required for the assemblies A0-A1 and collocation CO (middle left), and (iv) the relative wall times between A1 and A0 assemblies (right).

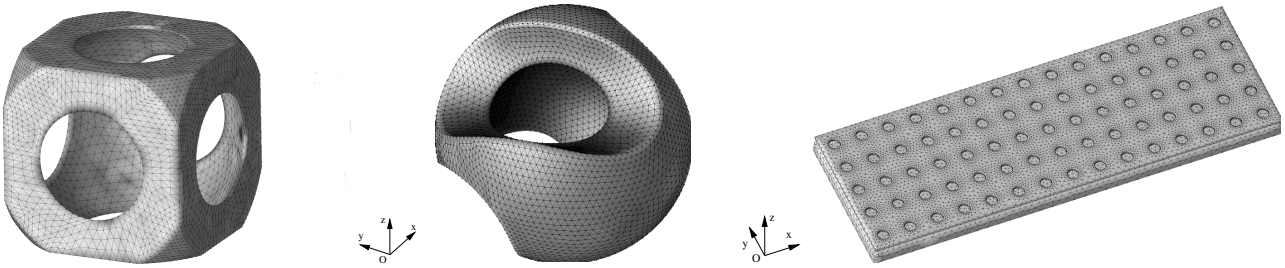

Fig. 5. Bodies with edges and corners: a hollow cube (HC) (left); a sculpted sphere (SS) (middle); and a perforated plate (PP) (right) [30].

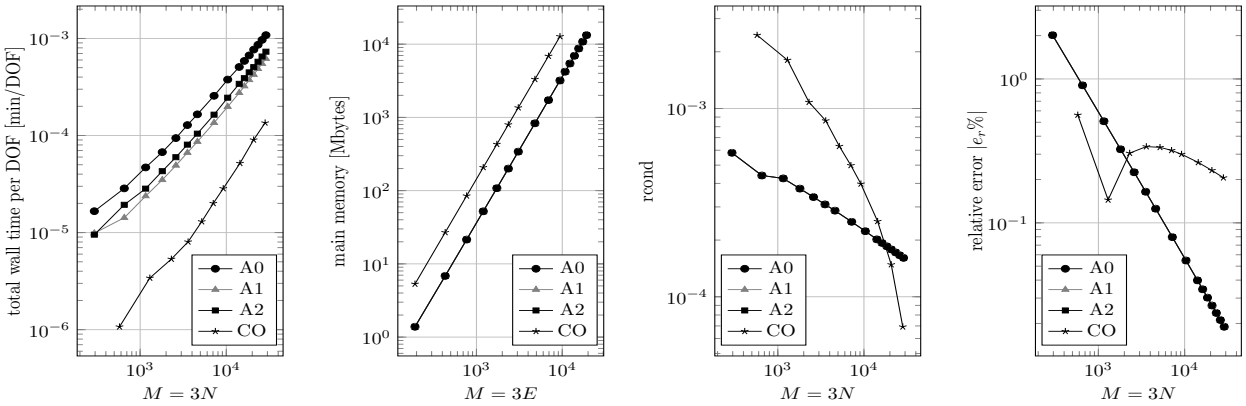

Fig. 6. Steady Stokes flow. Comparison between GBEM with assemblies A0-A2 and collocation CO in the unit sphere and using a Q_{22} quadrature, as functions of the degrees of freedom number $M = 3N$ or the number of elements E: (i) the total wall time per Degree Of Freedom (DOF) (left), (ii) the main memory in Mbytes (middle left), (iii) the reciprocal of the condition numbers of the system matrix rcond (middle right), and (iv) the relative errors $|e_r\%|$ in the Stokes force for steady creeping flow (right).

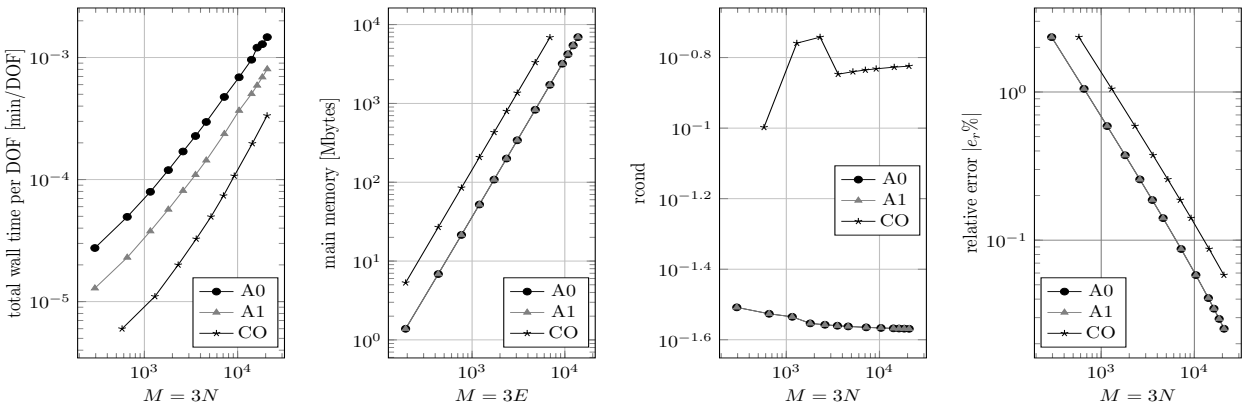

Fig. 7. Oscillatory Stokes flow. Comparison between GBEM with assemblies A0-A2 and collocation BEM (CO) in the unit sphere and using a Q_{22} quadrature, as functions of the degrees of freedom number $M = 3N$ or the number of elements E: (i) the total wall time per Degree Of Freedom (DOF) (left), (ii) the main memory in Mbytes (middle left), (iii) the reciprocal of the condition numbers of the system matrix rcond (middle right), and (iv) the relative errors $|e_r\%|$ in the Stokes force for steady creeping flow (right).

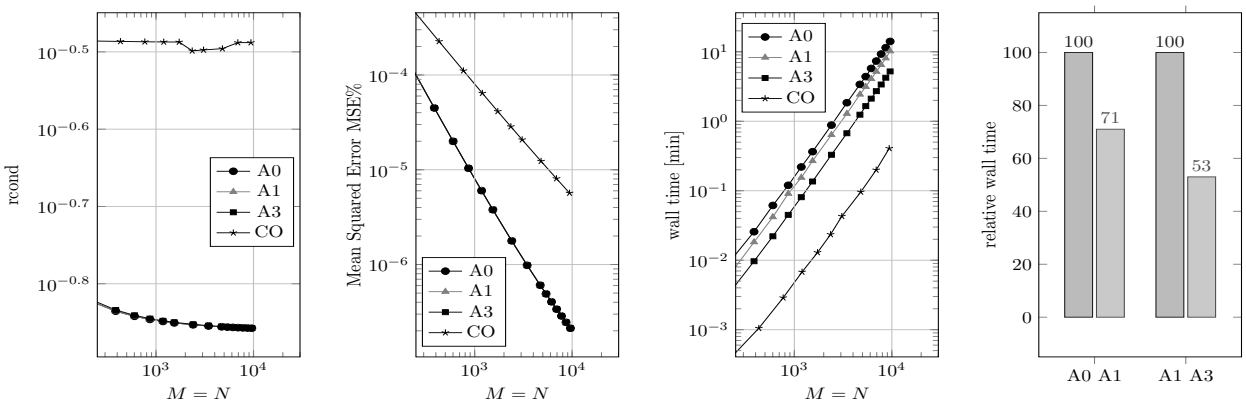

Fig. 8. Rankine closed body. Assemblies A0, A1, A3 and collocation CO, as functions of the degrees of freedom number $M = N$: (i) the reciprocal of the condition numbers of the system matrix rcond (left), (ii) the Mean Squared Error $\mathrm{MSE}\%$ in the dipolar density λ (middle left), (iii) the wall times required for assemblies A0, A1, A3, and collocation CO (middle right), and (iv) the relative wall times between the A1 and A0 assemblies, and between the A3 and A1 ones (right).

List of Tables

Table 1. Number of operations (by Gauss-Legendre quadrature point) in the assemblies A0, A1, and A2

product	A0 [Eqns. (21,22)]	A1 [Eqns. (21,24)]	A2 [Eqns. (24,25)]
	$3^2 \times 6 = 54$	$3^2 \times 2 = 18$	$6 \times 2 = 12$
	$3 \times 54 = 162$	not performed	not performed
	$162 + 3^2 \times 54 = 648$	$3^2 \times 18 = 162$	$3^2 \times 12 = 108$
relative count % w.r.t. A0	—	25 %	17 %
relative count % w.r.t. A1	—	—	67 %

Table 2. Wall times (in seconds) and relative times in assembling the system matrix for the Stokes flow around: a hollow cube (HC), a sculpted sphere (SS), and a perforated plate (PP)

	A0, Eqns. (21,22)			A1, Eqns. (21,24)			A2, Eqns. (24,25)		
	HC	SS	PP	HC	SS	PP	HC	SS	PP
wall time for assembly	436	655	2260	237	333	969	161	228	713
relative time % w.r.t. A0	—	—	—	54%	51%	43%	37%	32%	32%
relative time % w.r.t. A1	—	—	—	—	—	—	68%	69%	74%

Table 3. Integration coordinates $\boldsymbol{\mu}_n, \boldsymbol{\xi}_n$ and Jacobian J_n, as a function of the coordinates $0 \leq \omega, x, \chi_1, \chi_2 \leq 1$ in the case of the self–integrals $\boldsymbol{I_1} - \boldsymbol{I_3}$ [10, 11]

	$\boldsymbol{I}_1$	$\boldsymbol{I}_2$	$\boldsymbol{I}_3$
μ_1	ω	ωx	ωx
μ_2	ωx	$\omega(x-1)$	ω
ξ_1	$(1-\mu_1)\chi_1$	$(1-\mu_1+\mu_2)\chi_1-\mu_2$	$(1-\mu_2)\chi_1$ $+(\mu_2-\mu_1)$
ξ_2	$\xi_1\chi_2$	$(\xi_1+\mu_2)\chi_2-\mu_2$	$(\xi_1-\mu_2+\mu_1)\chi_2$
J_n	$(1-\mu_1)\xi_1$	$(1-\mu_1+\mu_2)(\xi_1+\mu_2)$	$(1-\mu_2)$ $\times(\xi_1-\mu_2+\mu_1)$

Table 4. Integration coordinates $\boldsymbol{\mu}_n$ and $\boldsymbol{\xi}_n$, as a function of the coordinates $0 \le \omega, x_1, x_2, \chi_1 \le 1$ in the integrals with a common edge $\boldsymbol{I}_4 - \boldsymbol{I}_9$ [10, 11]

n	μ_1	μ_2	ξ_1	ξ_2
4	$-\omega x_1$	$-\omega x_1 x_2$	$(1-\omega)\chi_1 + \omega$	$\omega(1 - x_1 + x_1 x_2)$
5	ωx_1	$\omega x_1 x_2$	$(1-\omega)\chi_1$	$\omega(1 - x_1)$
			$+\omega(1 - x_1)$	
6	$-\omega x_1 x_2$	$\omega x_1(1 - x_2)$	$(1-\omega)\chi_1 + \omega$	$\omega(1 - x_1)$
7	$\omega x_1 x_2$	$\omega x_1(x_2 - 1)$	$(1-\omega)\chi_1$	$\omega(1 - x_1 x_2)$
			$+\omega(1 - x_1 x_2)$	
8	$-\omega x_1 x_2$	$-\omega x_1$	$(1-\omega)\chi_1 + \omega$	ω
9	$\omega x_1 x_2$	ωx_1	$(1-\omega)\chi_1$	$\omega(1 - x_1)$
			$+\omega(1 - x_1 x_2)$	$\omega(1 - x_1)$

Table 5. Integration coordinates $\boldsymbol{\xi}_{10}$ and $\boldsymbol{\eta}_{10}$, as a function of the coordinates $0 \leq \omega, z_1, z_2, z_3 \leq 1$ in the integral with a common vertex $\boldsymbol{I}_{10}$ [10, 11]

	ξ_1	ξ_2	η_1	η_2
$\boldsymbol{I}_{10}$	ω	ωz_1	ωz_2	$\omega z_2 z_3$